SIMULTANEOUS REMOVAL OF NOX AND SO₂ WITH H₂O₂ OVER SILICA SULFURIC ACID CATALYST SYNTHESIZED FROM FLY ASH

[1]Qambarov Asadjon, [2]Abdujabborov Sultonbek, [3]Ochilov Mansur, [4]Shamatov Sirojiddin
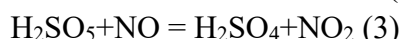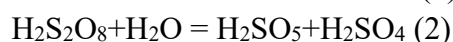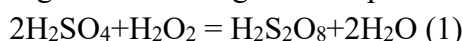[1234]Almalyk branch of Tashkent State Technical University named after I.A. Karimov

Abstract. Considering that the utilization of fly ash in the removal of flue gas pollutants not only provide a way of high value-added utilization of fly ash, but also greatly reduce the cost of removing flue gas pollutant, the synthesis of silica sulfuric acid catalyst from fly ash and its application in simultaneous removal of NOx and SO₂ with H₂O₂ were investigated in this work. Circulating fluidized bed boiler (CFB) fly ash and pulverized coal boiler (PC) fly ash were selected as raw material to prepare silica sulfuric acid catalyst by H₂SO₄ activation. PC fly ash was difficult to be activated by H₂SO₄ due to its dense structure, while CFB fly ash could be treated with H₂SO₄ to promote dealumination, thereby increasing the silica content. Moreover, the -SO₃H withdrawing groups were detected on the silica surface by XPS and Py-FTIR technologies, indicating the formation of silica sulfuric acid. Silica sulfuric acid showed higher activity in catalyzing the NO oxidation by H₂O₂, and a possible reaction mechanism was proposed. Combined with alkali absorption, 99% SO₂ and 92% NOx removal efficiencies can be achieved. The effects of activation conditions such as activation temperature, activation time and calcination temperature and removal experimental parameters such as H₂O₂ concentration, SO₂ concentration and simulated flue gas temperature on the catalytic performance were studied. Finally, the catalyst was not found to be deactivated for ten hours in the stability test.

Keywords: fly ash, Sulfuric acid, silica sulfuric acid, H₂O₂, denitrification, desulfurization.

Introduction. Uzbekistan is the world's largest producer and consumer of coal, and the exploitation of coal has caused serious damage to the ecological environment. Massive SO₂ and NOx emitted from coal-fired power plant boilers has become the one of the main source of air pollution (Ding et al., 2014). Furthermore, fly ash, as an industrial by-product of coal combustion in thermal power plants one of the most complex anthropogenic materials. It is estimated that the yield of fly ash produced in the word is more than 300 billion tons, but only a small part of which is used as cement and concrete materials (Wang and Wu, 2006). The improper disposal of fly ash has become an environmental issue and resulted in a waste of recoverable resources. At present, there is an urgent need to develop new ways of utilizing fly ash in order to safeguard the environment and provide cost-effective ways for large-scale utilization (Yao et al., 2015). If fly ash can be used in the removal of flue gas pollutants, it will be a promising way to use fly ash, because it not only saves the transport cost of fly ash, but also reduces the cost of flue gas pollutant removal.

Currently, wet flue-gas desulfurization technology (WFGD) and selective catalytic reduction (SCR) with NH₃ have been widely used in coal-fired power plants to achieve desulfurization and denitrification in coal-fired flue gas. However, the separate removal of SO₂ and NOx results in a lot of problems, such as serious dust deposition on the air-preheater, high

operating costs, low utilization of by-products, secondary pollution produced and large area occupied (Ye et al., 2014). Thus, developing a system for simultaneous removal of NOx and SO_2 has become one of the most widely concerned topics (Deng et al., 2013). Oxidation-absorption process has great advantages in many processes for simultaneous removal of NOx and SO_2 due to its simple system and low cost. But the key to this process is rapid oxidation of NO because NO is a stable radical species with a low ionization energy of 9.26 eV (Cui et al., 2019a, 2019b). The most common ways to oxide NO are by Advanced Oxidation Processes (AOPs), selective catalytic oxidation with O_2 and strong oxidant oxidation (Chen et al., 2013; Ding et al., 2015; Zhao et al., 2014). Among these processes, AOPs based on heterogeneous Fenton reaction is the most promising because the hydroxyl radicals generated during the Fenton reaction are extremely oxidizing and can instantly oxidize NO without the generation of secondary pollutants. In our previous work magnetic sphere in fly ash was successfully prepared as heterogeneous Fenton catalysts and applied in the simultaneous removal of NOx and SO_2 (Cui et al., 2018). It can achieve 90% NOx removal efficiency at 140 °C, with 0.07 mg/min and 2 mol/L of H_2O_2. But it is estimated that proportion of magnetic sphere in fly ash is only 0.5%-18% (Yang et al., 2014), which means that fly ash is not fully utilized. Unexpectedly, we found that sulfuric acid formed by the reaction of H_2O_2 and SO_2 attached to the wall of quartz tube reactor can catalyze the oxidation of NO by H_2O_2 without solid catalyst through the following reaction path.

$$2H_2SO_4+H_2O_2 = H_2S_2O_8+2H_2O \quad (1)$$
$$H_2S_2O_8+H_2O = H_2SO_5+H_2SO_4 \quad (2)$$
$$H_2SO_5+NO = H_2SO_4+NO_2 \quad (3)$$

Due to the strong oxidizing properties of H_2SO_4/H_2O_2 solution, it is used in surface chemical oxidation. Kazuyuki et al. found that the oxidation occurred immediately upon immersing the Si (1 1 1) surface in the solution (Kobayashi et al., 1996). Norio et al. suggested that the H_2SO_4/H_2O_2 solution was an effective wet-process for preparing atomically flat oxidized diamond (1 1 1) surface (Tokuda et al., 2009). H_2SO_4/H_2O_2 system shows potential utility in NO oxidation considering that SO2 in the flue gas can be oxidized by H_2O_2 to H_2SO_4 that can continue to participate in NO oxidation reaction as catalyst. In addition, H_2O_2 is an ideal oxidant because of an effective-oxygen content (47%), only water after oxidation reaction, safety in operation and storage and the low cost. (Shaabani and Rezayan, 2007). However, H_2SO_4/H_2O_2 solution presents limitations in NO oxidation due to the disadvantages in handling, corrosiveness, difficult workup and toxic waste (Vekariya et al., 2016). But the above problems can be avoid if H_2SO_4 is supported on a porous support and then catalyze the oxidation of NO with gas-phase H_2O_2. In organic reactions, SiO_2 is usually selected as the support of various mineral acids such as H_2SO_4 (Salehi et al., 2006), HF (Corro et al., 2010), $HClO_4$ (Mandal and Misra, 2006), H_3PO_4 (Maki et al., 1998). Silica supported mineral acids have attracted much attention due to high efficiency resulting from greater surface area, greater stability and reusability, low toxicity, greater selectivity, and ease of handling. Fly ash is a silica-aluminate material composed of silica, alumina, and FeOx as the major constituents and varying amount of CaO, MgO and SO_3 with unburned carbon. It was reported that fly ash can be chemically activated by strong acid treatment and the silica content of the fly ash is increased because most of the elements such as alumina and iron can be easily removed by the acid leaching method (Blanco et al., 2005). Therefore fly ash has great potential to be prepared as silica sulfuric acid by using sulfuric acid treatment.

In the present work, circulating fluidized bed boiler (CFB) fly ash and pulverized coal boiler (PC) fly ash were selected as raw material to prepare silica sulfuric acid by sulfuric acid activation. Physical and chemical properties of CFB and PC fly ash after sulfuric acid activation were comprehensively compared by using different techniques. In addition, the effects of acid activation temperature, acid activation time, and calcination temperature on silica sulfuric acid prepared from CFB fly ash were also investigated. Finally, NO removal efficiencies of the silica-supported sulfuric acid with gas-phase H_2O_2 were tested on a fixed bed reactor, and the possible reaction pathways, stability test and the effects of simulated flue gas temperature, H_2O_2 concentration, and SO_2 concentration on NO removal were discussed.

2. Experimental

2.1. Materials.

CFB fly ash was from Pingshuo thermal power plant (Shanxi Province, China) and PC fly ash was from Gongyi thermal power plant (Henan Province, China). They were named PS-FA and GYFA respectively. Hydrogen peroxide (H_2O_2, 30 wt% aqueous) was purchased from Tianjin ZhiYuan Reagent Co., Ltd. Nitric oxide (1% NO/N_2), sulfur dioxide (2% SO_2/N_2) and nitrogen were provided by Wuhan Newradar Special Gas Co, Ltd. Calcium hydroxide ($Ca(OH)_2$, 95%), Concentrated sulfuric acid (H_2SO_4, 98%) and Potassium permanganate ($KMnO_4$, 99.3%) were purchased from Sinopharm Chemical Reagent Co., Ltd. All chemicals were of analytical reagent (A.R.) grade. These were used as received without any further purification unless otherwise mentioned.

2.2. Catalyst preparation.

The synthesis of activated fly ash (AFA) was carried out by chemical activation of fly ash with concentrated H_2SO_4 at the solid to liquid ratio of 1 g: 10 mL, at 120 °C under N_2 flow, under constant stirring for 96 h. After aging, the mixture was washed with distilled water to remove leached compounds. The resulting solid was further dried at 120 °C for 24 h and calcined at 400 °C for 4 h under static condition. The obtained activated fly ash from PS-FA and GY-FA were named PS-AFA and GY-AFA respectively.

2.3. Characterization of catalyst.

Power X-ray diffraction (XRD) measurement was carried out with a Rigaku ULTIMA diffractometer at a scanning rate of 8 min^{-1} between 15 °C and 50 °C. The Fourier transformation infrared (FTIR) spectroscopy were recorded on a Bruker spectrometer by dispersing the samples in KBr pellets with 4 cm^{-1} resolution. The morphologies of the samples were characterized using fieldemission scanning electron microscopy (Tescan Mira 3) at a voltage of 20 kV. The specific surface areas of the samples were calculated by the Brunauer-Emmett-Teller (BET) method with a Micromeritics ASAP 2020 volumetric apparatus. The elemental composition of the samples was studied with X ray fluorescence spectroscopy (XRF) using PAN analytical Epsilon1 apparatus. The differential scanning calorimetry (DSC) and thermogravimetric (TG) analysis were performed in NETZSCH STA449F5. The X-ray photoelectron spectroscopy (XPS) was carried out on a Thermo ESCALAB 250X (America) electron spectrometer using 150 W Al Ka X-ray source. The acidity of the samples was measured by ammonia temperature-programmed desorption (NH_3-TPD-MS). The acid sites (Brønsted or Lewis) of the samples were determined by FTIR studies using pyridine as a probe in a Nicolet-380 spectrophotometer and spectra were recorded in the range of 1400 – 1600 cm^{-1} .

2.4. Catalytic performance test.

As shown in Fig. S1, the experiments were conducted on a fixedbed system, which consisted of the generation of simulated flue gas, the H_2O_2 atomization, the oxidation of NO and SO_2 and the detection and absorption of oxidation products. The total flow was 250 mL/min and the simulated flue gases were supplied by compressed gas cylinders filled with NO, SO_2 and N_2, which were metered through a mass flow controller and mixed in buffer bottle. The atomized H_2O_2 was produced by a self-made ultrasonic H_2O_2 atomizer and carried into the reaction tube by N_2. The flow of H_2O_2 can be adjusted by the volume flow of carrier gas N_2. Different concentration of H_2O_2 can be obtained by diluting 30% H_2O_2 with deionized water. Oxidation was carried out in fixed bed reactor made of quartz, which was equipped with a quart diaphragm to support the catalyst, and the temperature was measured by a K-type thermocouple. The oxidation products of SO_2 and NOx were absorbed in an airtight glass bottles filled with saturated calcium hydroxide solution. The concentration of residual NO was detected by the flue gas analyzer (Testo 350). The catalyst was 0.2 g. NO and SO_2 removal efficiency was obtained after 1 h at steady state by the following equation (4). g was the removal efficiency, Cin and Cout was the inlet and outlet of NO and SO_2 concentration. The value was tested for three times by using Testo 350 portable emission analyzer.

$$\eta = \frac{Cin - Cout}{Cin} * 100\%$$

3. Result

3.1. Catalyst characterization

The chemical composition of samples is given in Table 1. As can be seen from Table 1, the main components of PS-FA and PC-FA were SiO_2, Al_2O_3, CaO and Fe_2O_3, and the total amount of SiO_2 and Al_2O_3 accounted for more than 75%. Therefore, GY-FA and PS-FA were usually classified as type F according to ASTM C-618 (Diaz et al., 2010). The content of CaO and SO_3 in PS-FA were higher than that of GY-FA, which is because the fluidized bed boiler need to simultaneously fix sulfur using sulfur-fixing agent ($CaCO_3$) in the combustion process. For PS-FA. The SiO_2 content after acid activation increased from 39.1% to 75.8%, while the Al_2O_3 content decreased from 35.9% to 18.9%. For GY-FA, the SiO_2 content after acid activation enhanced from 51.6% to 58%, while the Al_2O_3 content decreased from 30.4% to 30.3%. It was apparent that the increase of the SiO_2/Al_2O_3 in PS-FA was higher than that of GYFA after acid activation, which indicating that the alumina in PSFA was more easily leached by sulfuric acid than GY-FA. Furthermore, components like FeOx, CaO and SO_3 of both fly ashes were also leached after acid treatment. However, a part of these components in GY-FA were wrapped by a structured dense siliconaluminum shell, which may be the reason why the content of these components in GY-AFA was higher than that of PS-AFA (Yang et al., 2017). The XRD patterns of samples in Fig. 1(a) show that PC fly ash was crystalline with prominent phases of mullite and quartz and FBC fly ash was also crystalline with prominent phases of quartz, hematite, lime and $CaSO_4$. For PS-FA, after acid activation, though the quartz phase was still predominant, the crystal size of quartz was reduced from 58 nm to 44 nm due to increasing content of amorphous silica. It is reported that the defect or disorder of the catalyst caused by the amorphous nature can makes the active center more easily exposed to the catalytic reaction (Goldsmith et al., 2017). The crystal size of quartz was calculated from Scherrer's equation considering the highest peak at $2h = 26. 6$. In addition, $CaSO_4$, hematite and lime phase almost disappeared in XRD patterns of PS-AFA. For GY-FA, there is basically no change in the mullite and quartz phase before and after acid activation. This result

was consistent with that of XRF. Comparing the GY-AFA and PS-AFA, we can find that PC fly ash has stronger resistance to concentrated H_2SO_4 than CFB fly ash. This is because the combustion temperature of the coal-fired boiler is relatively high, the glass body in the fly ash has a high degree of polymerization and undergoes a slow cooling process, resulting in the dense structure and stable surface of the glass body in the fly ash. FTIR spectra of samples are displayed in Fig. 1(b). The FTIR spectrum of all samples shows a broad band between 3000 and 3800 cm^{-1}, which is assigned to hydroxyl groups of physically adsorbed water molecules on the surface (Khatri and Rani, 2008). The broadness of the band was related to the strong hydrogen bonding between the hydroxyl groups. The peak at 1639 cm^{-1} was attributed to bending mode of water molecule. The absorption range of the OASAO asymmetric and symmetric stretching modes lies in 1120–1230 and 1010–1080 cm^{-1} respectively (Niknam et al., 2010). The bands at 1089 and 573 cm^{-1} in spectrum of all samples can be assigned to asymmetric SiAOASi and SiAOAAl stretching, the bands at 798 and 456 cm^{-1} were attributed to symmetric SiAOASi stretching and OASiAO bending vibrations, respectively (Mazumder et al., 2015). Comparing the FTIR spectra of GY-FA and GY-AFA, no obvious changes can be observed. However, the increased amorphous silica in PS-AFA can be characterized by an intense band in the bands at 1089, 798 and 456 cm^{-1} which were corresponded to the valence vibrations of silicate oxygen structure. In addition, the bands in the range 1120–1230 and 1010–1080 cm1 of PS-AFA related to OASAO asymmetric and symmetric stretching modes became more prominent than that of PS-FA, indicating that there is sulfuric acid attached to the surface of PS-AFA. Moreover, the intensity of the peaks at 3472 and 1639 cm1 of PS-AFA corresponding to the hydroxyl groups of physically adsorbed water molecules was increased, suggesting that the water absorption of PS fly ash was also significantly improved after acid activation. This was because $-SO_3H$ groups in sulfuric acid adsorbed on the surface of PS-AFA could be strongly hydrogen-bonded with the absorbed water molecules. The SEM images of the samples are given in Fig. S2. As can be seen from Fig. S2(a) and (c), there was a very obvious difference between the morphology of the CFB fly ash and that of PC fly ash. The PC fly ash were predominantly spherical in shape, and the surface of spherical microbeads was smooth. A small number of irregularly shaped particles can be seen from PC fly ash, which were assigned to glass slag or unburned carbon. CFB fly ash mainly contained irregularly shaped particles, and almost did not contain spherical particles. This is mainly because that the combustion temperature of CFB boiler is 850–900 °C, at which most minerals can only be softened without melting and further chemical reaction. Therefore, it was difficult to form spherical microbeads. From Fig. S2(b), some small holes appeared on the surface of individual spherical particles of PC fly ash after acid activation, but the morphology of most PC fly ash did not change due to the excellent acid resistance. Expectedly, CFB fly ash became loose and porous after acid activation from Fig. S2(d). The reason is that the components.

Samples	Composition						
	SiO_2	Al_2O_3	FeO_x	CaO	SO_3	TiO_2	Others
GY-FA	51.6	30.4	4.8	6.1	0.9	1.1	5.1
GY-AFA	58.0	30.3	4.0	2.4	0.1	1.0	4.2
PS-FA	39.1	35.9	4.7	8.9	6.9	1.0	3.5
PS-AFA	75.8	18.9	1.8	0.6	0.4	0.5	2.0

Fig. 1. (a) XRD patterns and (b) FTIR profiles of PS-FA, PS-AFA, GY-FA and GY-AFA.
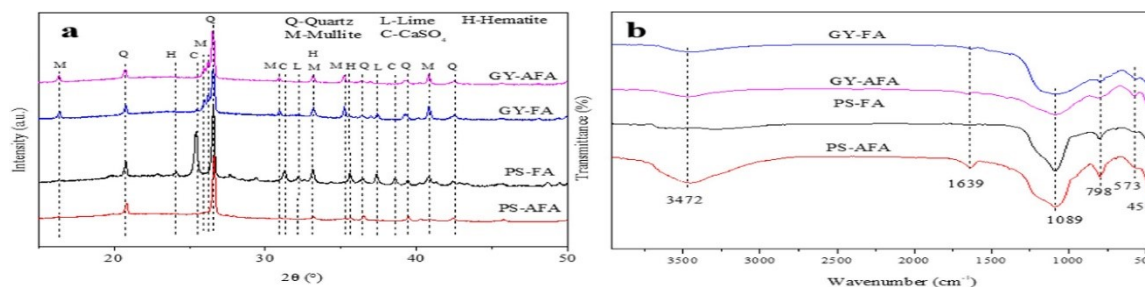
Fig. 1. ***(a) XRD patterns and (b) FTIR profiles of PS-FA, PS-AFA, GY-FA and GY-AFA.***

like Al_2O_3, FeO_x, CaO and SO_3 in fly ashes leached out during acid treatment.

The N_2 adsorption-desorption isotherms of GY-AFA and PS-AFA are shown in Fig. S3(a). The curve of the pore size distribution, which were calculated from the adsorption branches using the NLDFT model, are shown in Fig. S3(b). As shown in Fig. S3(a), the N_2 adsorption-desorption isotherms of the GY-AFA are type IV iso- therms with hysteresis loop of type H3, and the PS-AFA exhibited isotherms very closed to type IV with hysteresis loops of H4 shape according to the IUPAC nomenclature (Wang et al., 2014). PS-AFA showed a steep nitrogen uptake at very low relative pressures, which is corresponding to the filling of micropores. For both sam- ples, the hysteresis loop (p/p0:0.5–0.95) was attributed to the mesoporous nature of the material with slit shaped or panel shaped pores. As shown in Fig. S3(b), the pore size range of PS- AFA was mostly distributed between 0 and 2 nm, while the pore size range of GY-AFA was mostly distributed between 2 and 50 nm, suggesting that the former contained more micropores and the latter contained more mesopores. From Table S1 we can know that the specific surface area and pore volume of PS-AFA were 172.16 m^2/g and 0.14 cm^3/g, respectively, significantly higher than 6.8 m^2/g and 0.01 cm^3/g of GY-AFA. This was very beneficial for the catalytic or adsorption reaction. The XPS spectra of samples have been shown in Fig. 2. In case of Fig. 2(a), the binding energies of 102 eV and 102.8 eV were corre- sponding to the Si-O bands of SiO and Si-O-Al which were sub- oxides of silicon, and the binding energy (BE) of 103.5 eV was assigned to the Si-O bands of native oxide SiO_2 (Blandin et al., 2013; Gao et al., 2015; Lei and Gu, 2015). But it can be seen that a higher BE peak was appeared at 104.4 eV in Si 2p of PS-AFA which was attributed to Si-O bands of silica sulfuric acid (Ghoreishi et al., 2014). This was consistent with the FTIR result, indicating that there was indeed sulfuric acid adsorbed on the sur- face of PS-AFA through chemical bonds instead of physical adsorption. ASO_3H groups of silica sulfuric acid, as electron withdrawing group, can reduce electron cloud density of Si, resulting in higher Si 2p binding energy (Kore and Srivastava, 2012). As shown in Fig. 2 (b), the O 1s spectra of GY-FA and PS-FA were deconvoluted into three peaks. The low BE peak centered at about 531.0 eV was attributed to FeAO in FeO_x (Cui et al., 2018). The peak at about 531.9 eV came from the SiAOAAl bonds. And the high BE peak was located at about 532.7 eV, corresponding to the SiAO in SiO_2 (Gao et al., 2015). The BE peak at 533.5 eV in both GY-AFA and PS-AFA were corresponded to oxygen of adsorbed H_2O (Zhanget al., 2018). This was due to that the porous structure and surface ASO_3H groups increased their ability to adsorb water. In addition, the BE peak at about 534.2 eV of PS-AFA was assigned to oxygen of Si-O-S. In Fig. 2 (c), the binding energies 74.0 eV, 74.7 eV and 75.3 eV of Al 2p correspond to AlAO in alumina silicate, AlAOAC and Al_2O_3, respectively (Hu et al., 2015; Kovacich and Lichtman, 1985; Wang et al., 2015). In Fig.

2(d), the binding energies 710.3 eV, 711.4 eV and 713.3 eV of Fe 2p correspond to Fe^{2+} and Fe^{3+} in FeOFe and Fe^{3+} in FeOAl, respectively (Huang et al., 2015). It can be seen from Fig. 2(c, d) that the Fe 2p XPS feature of PS- AFA and GY-AFA almost disappeared, and the Al 2p XPS feature of PS-AFA was greatly weakened.

The surface elemental composition of PS-FA, PS-AFA, GY-FA and GY-AFA are present in Table 2. For PS fly ash, it is apparent that the Si in SiO and SiAOAAl was basically transformed into SiO_2 after acid activation, and about half of the SiO_2 acted as the support of silica sulfuric acid. But in case of GY fly ash, only a small part of Si in SiO and SiAOAAl was transformed into SiO_2 after acid activa- tion, and no silica sulfuric acid was found. With respect to O 1s, after the acid activation, the ratios of O/SiO_2 to O/AlAOASi in PS and GY fly ash decreased from 1.08 and 0.74 to 2.47 and 0.70, respectively. This again demonstrated that the Si/Al of PS-FA increased after acid activation due to the leaching of alumina. In the meanwhile, the ratios of O/FeOx decreased because the iron oxide on the surface of both PS and GY fly ash was leached by sulfuric acid. 16.8% of O/SAO in PS-AFA proved the existence of silica sulfuric acid.

The NH_3-TPD profiles of samples are displayed in Fig. 3(a). The NH_3-TPD profiles of the PS-FA and GY-FA clearly indicates two peaks, one between 300 and 500 °C and another relatively low- intensity peak at about 600 °C, indicating the presence of strong acidity due to ASO_4 groups (Lathiya et al., 2019). However, these two strong acidity peaks almost disappeared after acid activation from the NH_3-TPD profiles of the PS-AFA and GY-AFA. This may be because sulfates in fly ash can be dissolved and converted into bisulfate by concentrated sulfuric acid. In contrast to GY-AFA, PS- AFA showed one low temperature desorption peak at 150 °C which was attributed to weak acid sites. In Fig. 3(b), the FTIR spectra of pyridine adsorbed are shown over PS-AFA and GY-AFA. The PS-AFA presents a strong Lewis acid site as it can be seen with the intense vibrations at 1440 and 1450 cm^{-1} and no characteristic Brønsted band was observed. Moreover, the strong Lewis acid site was assigned to the silica sulfuric acid due to the electron-withdrawing properties of the ASO_3H groups (Corro et al., 2010;
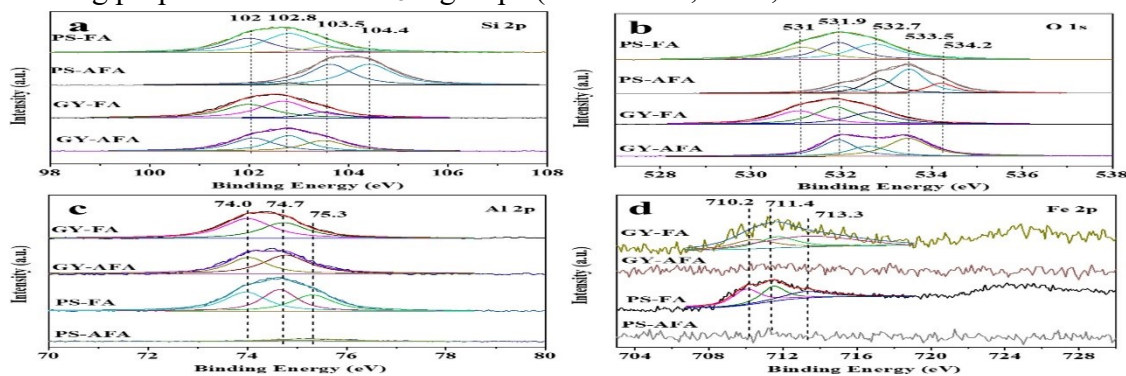

Fig. 2. XPS spectra of (a) Si 2p, (b) O 1s, (c) Al 2p and (d) Fe 2p of PS-FA, PS-AFA, GY-FA and GY-AFA.

Manríquez et al., 2004). Generally, the NH_3 desorption peaks at lower temperature are mainly related to Lewis acid sites, and the peaks at higher temperature correspond to Brønsted acid sites (Jin and Li, 2009). Therefore, the results of NH_3-TPD was consistent with the results of FTIR spectra of pyridine.

The thermal analysis was conducted In order to determine the thermal stability of the samples. Fig. 3(c) presents the results of TG of samples. The results are shown on the basis of a temperature increase function of up to 700 °C.

Table 2 Surface elemental composition of PS-FA, PS-AFA, GY-FA and GY-AFA by XPS.

Samples	Atomic Concentration						
	Si 2p					0 1S	
	Si/SiO	Al_2O_3	FeO_x	CaO	SO_3	TiO_2	Others
GY-FA	51.6	30.4	4.8	6.1	0.9	1.1	5.1
GY-AFA	58.0	30.3	4.0	2.4	0.1	1.0	4.2
PS-FA	39.1	35.9	4.7	8.9	6.9	1.0	3.5
PS-AFA	75.8	18.9	1.8	0.6	0.4	0.5	2.0

As can be seen in Fig. 3(c), as raw materials, the TG curves of GY-FA and PS-FA were completely dif- ferent, indicating the difference in their chemical properties. GY-FA was relatively stable, and the total mass loss of GY-FA was no more than 0.2%. However, PS-FA demonstrated 2.6% and 1.2% of mass loss at 30–500 °C and 500–700 °C, respectively. The former was responded to the loss of water molecules, in which the mass loss at below 200 °C was attributed to the release of surface free water molecules, and the mass loss at between 200 and 500 °C was due to the evaporation of crystallized water (Chatterjee et al., 2018). The latter was assigned to the thermal dissociation of $CaCO_3$ (Grela et al., 2016). After acid activation, the overall mass loss of GY- AFA was 0.5%, slightly higher than that of GY-FA. The overall mass loss of PS-AFA was 3.8%, same to that of PS-FA. Nevertheless, the mass loss trend of PS-AFA with temperature was different from that of PS-FA. At the stage of losing free water, the mass loss of PS-AFA was 2.5%, significantly higher than 1.2% of PS-FA, due to the surface -SO_3H groups of PS-AFA. But at the stage of losing struc- tural water, the mass loss of PS-AFA was 0.5%, lower than that of PS-FA. This may be because the acid activation has leached out the inorganic salts with structured water. It is worth noticing that although PS-AFA no longer contained $CaCO_3$ after acid activation, 0.7% of mass loss was still observed at above 500 °C, which may be due to the decomposition of silica sulfuric acid.
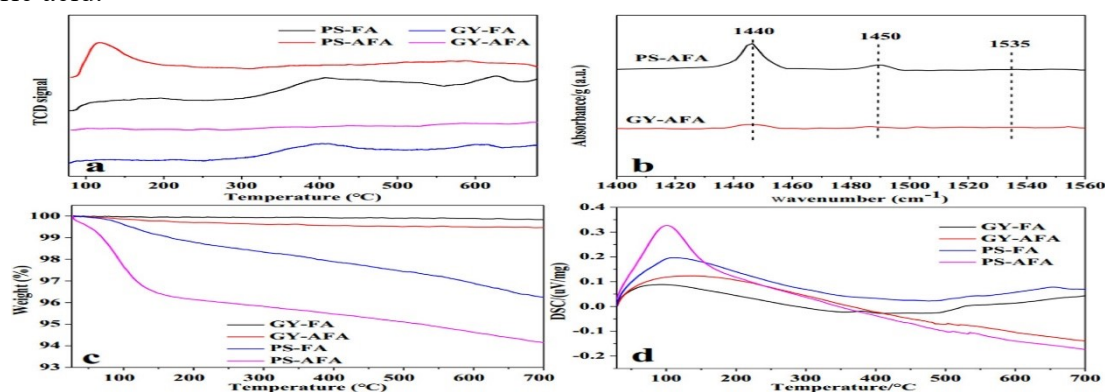

Fig. 3. (a) NH3-TPD profiles; (b) FTIR spectra of Pyridine adsorbed; (c) TG profiles and (d) DSC profiles of PS-FA, PS-AFA, GY-FA and GY-AFA.

3.2. Effect of activation time, activation temperature and calcination temperature.

In order to further investigate the effect of activation time, activation temperature and calcination temperature on catalytic performance, PS-FA was activated under activation time, activation temperature and calcination temperature, and the FTIR profiles and TG profiles of which are presented in Fig. 4. The effect of acid activation condition can be seen combining the FTIR profiles and TG profiles. In terms of activation time, the intensities of peaks at 798 and 456 cm^{-1} which were assigned to symmetric SiAOASi stretching and OASiAO bending vibrations became stronger with the extension of activation time. This suggested that more and more silica was generated from silicate or exposed due to the leaching of alumina. In addition, the intensities of peaks at 3472
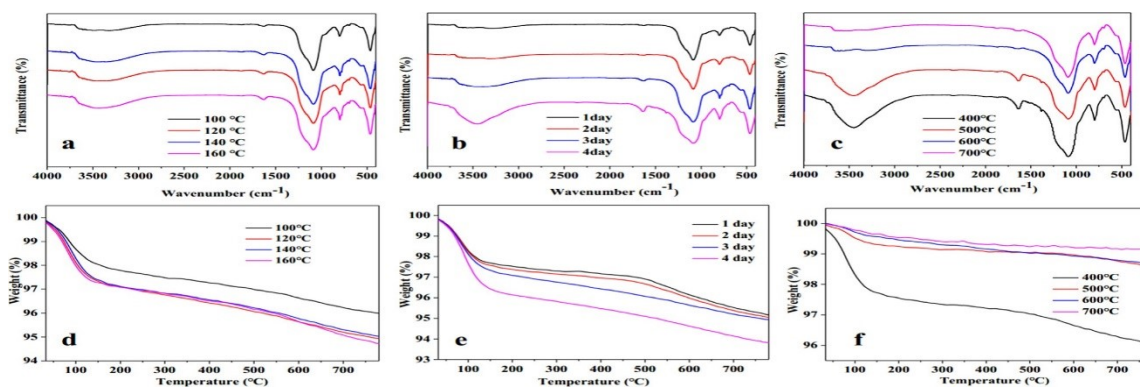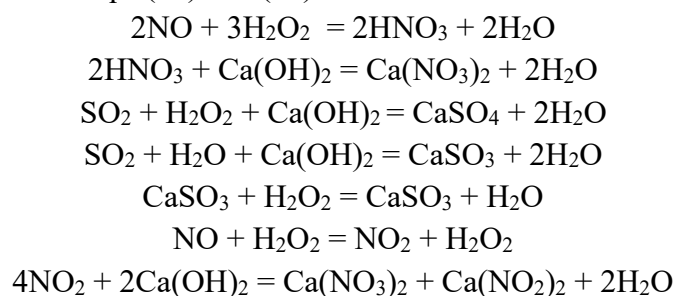

Fig. 4. FTIR profiles of PS-AFA obtained by acid activation under different (a) activation time, (b) activation temperature and (c) calcination temperature and TG profiles of PS- AFA obtained by acid activation by different (d) activation time, (e) activation temperature and (f) calcination temperature.

and 1639 cm^{-1} which were assigned to water molecule became stronger with the extension of activation time, which was due to that more water was attached to PS-AFA. From Fig. 4(d), it can be observed that the mass loss rate of PS-AFA in the 30–200 °C range which was attributed to the mass loss of surface free water increased with the extension of time. This again demonstrated that prolonging the activation time can increase the number of porous structures and -SO$_3$H groups of the material. As shown in Fig. 4(b) and (e), the activation temperature had little effect on the acid acti- vation when the temperature increased from 120 to 160 °C. With respect to the effect of calcination temperature, it can be found that the AOH bands of water intensity has considerably dimin- ished when PS-AFA was calcined at above 500 °C from Fig. 4(c). The mass loss of surface free water was drastically reduced when PS-AFA was calcined at above 500 °C from Fig. 4(f), resembling the results of FTIR analysis. According to Fig. 3(c), one likely expla- nation is that silica sulfuric acid started to decompose at 500 °C. The mass loss rates of PS-AFA calcined at 600 and 700 °C at above 500 °C was less than that of PS-AFA calcined at 400 and   500 °C, which again proved the water adsorption was reduced due to the decomposition of silica sulfuric acid.

3.3.   Catalytic performance in simultaneous removal of NO and SO$_2$. The comparison of NO and SO$_2$ removal efficiencies of raw fly ash and acid activated fly ash under different condition is listed in Table 3. As a blank experiment Test 1, the removal efficiency of H$_2$O$_2$ was tested separately before the catalysts was added. As can be seen in Table 3, NO removal efficiency of H$_2$O$_2$ was only 9% due to weak oxidizing property, and the removal reaction equa- tions are shown in Eqs. (5) and (6). However, SO$_2$ removal effi ciency was 99%, and the removal reaction equations are shown in Eqs. (7)–(9). GY and PS raw fly ash show 10% and 9% of NO removal efficiency, respectively, indicating that both PS-FA and GY-FA did not have the ability to catalyze

the oxidation of NO with H_2O_2. After activation, GY-AFA and PS-AFA showed catalytic activity, and their NO removal efficiency increased from 10% and 9% to 17% and 64%. This suggested that some groups on activated fly ash have played a role in catalysis, and the content of this groups in PS-AFA was much higher than that in GY-AFA. According to the results of FTIR, XPS, TG and Py-FTIR, silica sulfuric acid was considered as the active component of the catalytic reaction. To further confirm this judgment, PS-AFA obtained by acid activation under different activation time, activation temperature and calcination temperature were used for NO removal experiments, and the results are shown in Table 3 (Test 8–16). Combined with the FTIR and TG profiles of PS-AFA displayed in Fig. 4, we can find that the NO removal efficiency of PS-AFA was directly proportional to the amount of silica sulfuric acid in catalysts, which once again illustrated that silica sulfuric acid was the active component of the catalytic reaction.

In order to investigate the reaction mechanism of catalytic oxi- dation of NO by silica sulfuric acid, radical scavenger test were con- ducted. Considering that only hydroxyl radical was the most oxidizing among the free radicals decomposed by H_2O_2. Iso- propanol (IP), as a kind of hydroxyl radical scavenger, was selected for scavenger test. Before scavenger test, 99 wt% IP was added into the prepared H_2O_2 solution, so that the concentration of IP was 20% by changing the amount of 99 wt% IP. From Test 7, there was almost no reduction in NO removal efficiency, which showed that no hydroxyl radicals were generated during the catalytic reaction, that is, NO was not oxidized by the hydroxyl radicals. To further explore the mechanism, NO removal experiment (Test 6) was repeated without IP in the reactor 2, whose schematic diagram was shown in Fig. S4. Comparing the result of Test 5 and Test 6, it can be found that NO could be oxidized only when NO and H_2O_2 were co-adsorbed on the PS-AFA. Based on the above analysis and referring to previous reports (Jafari et al., 2012), we proposed that a reaction mechanism of silica sulfuric acid catalyzing the oxi- dation of NO by H_2O_2 as illustrated in Scheme S1. The $-SO_3H$ groups described in Scheme S1 are electron-withdrawing groups and H_2O_2 can act as an electron-donating groups, so they reacted to form ASO_4H groups and H_2O. Then SiO_2AOSO_4H oxidized NO to NO_2, and at the same time it turned back to SiO_2AOSO_3H. The NO removal reaction catalyzed by silica sulfuric acid were shown in Eqs. (10) and (11).

$$2NO + 3H_2O_2 = 2HNO_3 + 2H_2O$$
$$2HNO_3 + Ca(OH)_2 = Ca(NO_3)_2 + 2H_2O$$
$$SO_2 + H_2O_2 + Ca(OH)_2 = CaSO_4 + 2H_2O$$
$$SO_2 + H_2O + Ca(OH)_2 = CaSO_3 + 2H_2O$$
$$CaSO_3 + H_2O_2 = CaSO_3 + H_2O$$
$$NO + H_2O_2 = NO_2 + H_2O_2$$
$$4NO_2 + 2Ca(OH)_2 = Ca(NO_3)_2 + Ca(NO_2)_2 + 2H_2O$$

4. Conclusion

In the present study, an efficient and cost-effective silica sulfu- ric acid catalyst was synthesized by chemically activating CFB fly ash using concentrated sulfuric acid. However, PC fly ash did not have the advantage of being prepared as silica sulfuric acid catalyst due to its dense silicon-aluminum shell which was difficult to be activated by concentrated sulfuric acid. The chemical activation of CFB fly ash decreased the alumina content and increased the silica content. The characterization of the catalyst confirmed the loading of sulfuric acid on activated CFB fly ash surface. The pre- pared catalyst had a large specific surface area and possesses amount of Lewis acidity. The effect of activation temperature, acti- vation time and calcination temperature

on CFB fly ash were also studied. The results showed that prolonging the activation time can increase the activation effect, but increasing the temperature from 120 to 160 °C did not greatly improve the activation effect, and the catalyst will be deactivated when the calcination temperature exceeded 500 °C due to the decomposition of surface active components (ASO_3H).

Moreover, the application of activated CFB fly ash as catalyst for the simultaneous removal of SO_2 and NOx was proposed and pro- ven feasible. 99% SO_2 and 92% NOx removal efficiencies were achieved with 2 mol/L and 5 mL/h H_2O_2 at 140 °C, and the possible removal mechanisms were proposed. The effects of simulated flue gas temperature, H_2O_2 concentration, and SO_2 concentration on NO removal efficiency were discussed. The NO removal efficiency increased first and then decreased with the increase of SO_2 concentration and simulated flue gas temperature and it first increased and then remained basically unchanged with the increase of H_2O_2 concentration. Finally, the catalyst was not found to be deactivated for ten hours in the stability test, and no obvious change was observed in the XPS characterization before and after the reaction, indicating that the catalyst had good catalytic stability.

REFERENCES

1. Blanco, F., Garcia, M.P., Ayala, J., 2005. Variation in fly ash properties with milling and acid leaching. Fuel 84, 89–96.
2. Blandin, P., Maximova, K.A., Gongalsky, M.B., Sanchez-Royo, J.F., Chirvony, V.S., Sentis, M., Timoshenko, V.Y., Kabashin, A.V., 2013. Femtosecond laser fragmentation from water-dispersed microcolloids: toward fast controllable growth of ultrapure Si-based nanomaterials for biological applications. J. Mater. Chem. B 1, 2489.
3. Chatterjee, A., Hu, X., Lam, F.L.-Y., 2018. Catalytic activity of an economically sustainable fly-ash-metal-organic- framework composite towards biomass valorization. Catal Today 314, 137–146.
4. Chen, J., Shen, M., Wang, X., Wang, J., Su, Y., Zhao, Z., 2013. Catalytic performance of NO oxidation over $LaMeO_3$ (Me = Mn, Fe, Co) perovskite prepared by the sol–gel method. Catal Commun 37, 105–108.
5. Corro, G., Tellez, N., Ayala, E., Marinez-Ayala, A., 2010. Two-step biodiesel production from Jatropha curcas crude oil using SiO_2 HF solid catalyst for FFA esterification step. Fuel 89, 2815–2821.
6. Cui, R., Ma, S., Wang, J., Sun, S., 2019a. NO oxidation over Fe-based catalysts supported on montmorillonite K10, c-alumina and ZSM-5 with gas-phase H_2O_2. Chemosphere 234, 302–309.
7. Cui, R., Yang, B., Li, S., Wang, J., Ma, S., 2018. Heterogeneous Fenton catalysts prepared from modified-fly ash for NOx removal with H_2O_2. Catal Commun.
8. Cui, R., Yang, B., Li, S., Wang, J., Ma, S., 2019b. Heterogeneous Fenton catalysts prepared from modified-fly ash for NOx removal with H_2O_2. Catal Commun. 119, 180–184.
9. Deng, H., Yi, H., Tang, X., Liu, H., Zhou, X., 2013. Interactive effect for simultaneous removal of SO_2, NO, and CO_2 in flue gas on ion exchanged zeolites. Ind. Eng. Chem. Res. 52, 6778–6784.
10. Diaz, E.I., Allouche, E.N., Eklund, S., 2010. Factors affecting the suitability of fly ash as source material for geopolymers. Fuel 89, 992–996.

11. Ding, J., Zhong, Q., Zhang, S., Cai, W., 2015. Size- and shape-controlled synthesis and catalytic performance of iron-aluminum mixed oxide nanoparticles for NOx and SO$_2$ removal with hydrogen peroxide. J. Hazard Mater. 283, 633–642.

12. Ding, J., Zhong, Q., Zhang, S., Song, F., Bu, Y., 2014. Simultaneous removal of NOx and SO$_2$ from coal-fired flue gas by catalytic oxidation-removal process with H$_2$O$_2$. Chem. Eng. J. 243, 176–182.

13. Gao, J., He, G., Zhang, J.W., Deng, B., Liu, Y.M., 2015. Annealing temperature modulated interfacial chemistry and electrical characteristics of sputtering- derived HfO$_2$/Si gate stack. J. Alloy Compd. 647, 322–330.

14. Ghoreishi, K.B., Asim, N., Yarmo, M.A., Samsudin, M.W., 2014. Mesoporous phosphated and sulphated silica as solid acid catalysts for glycerol acetylation. Chem. Pap. 68, 1194–1204.

15. Goldsmith, B.R., Peters, B., Johnson, J.K., Gates, B.C., Scott, S.L., 2017. Beyond ordered materials: understanding catalytic sites on amorphous solids. ACS Catal. 7, 7543–7557.

16. Grela, A., Łach, M., Mikuła, J., Hebda, M., 2016. Thermal analysis of the products of alkali activation of fly ash from CFB boilers. J. Therm. Anal. Calorim. 124, 1609– 1621.

17. Huang, X., Ding, J., Zhong, Q., 2015. Catalytic decomposition of H$_2$O$_2$ over Fe-based catalysts for simultaneous removal of NOx and SO$_2$. Appl. Surf. Sci. 326, 66–72.

18. Hu, X., Yu, Y., Zhou, J., Wang, Y., Liang, J., Zhang, X., Chang, Q., Song, L., 2015. The improved oil/water separation performance of graphene oxide modified Al$_2$O$_3$ microfiltration membrane. J. Membrane Sci. 476, 200–204.

19. Jafari, H., Rostami, A., Ahmad-Jangi, F., Ghorbani-Choghamarani, A., 2012. Sulfamic acid-catalyzed oxidation of sulfides to sulfoxides and sulfones using H$_2$O$_2$: green and chemoselective method. Synthetic Commun. 42, 3150–3156.

20. Jia, Y., Zhong, Q., Fan, X., Wang, X., 2010. Kinetics of oxidation of total sulfite in the ammonia-based wet flue gas desulfurization process. Chem. Eng. J. 164, 132– 138.

21. Jin, F., Li, Y., 2009. A FTIR and TPD examination of the distributive properties of acid sites on ZSM-5 zeolite with pyridine as a probe molecule. Catal. Today 145, 101–107.

22. Khatri, C., Rani, A., 2008. Synthesis of a nano-crystalline solid acid catalyst from fly ash and its catalytic performance. Fuel 87, 2886–2892.

23. Kobayashi, K., Unno, H., Takizawa, H., Adachi, S., 1996. Chemical treatment effect of Si(111) surfaces in H$_2$SO$_4$: H$_2$O$_2$ solution. Jpn. J. Appl. Phys. 35, 5925–5928.

24. Kovacich, J., Lichtman, D., 1985. A qualitative and quantitative study of the oxides of aluminum and silicon using AES and XPS. J. Electron. Spectrosc. 35, 7–18.

25. Kore, R., Srivastava, R., 2012. Influence of -SO$_3$H functionalization (N-SO$_3$H or NR- SO$_3$H, where R= alkyl/benzyl) on the activity of Brönsted acidic ionic liquids in the hydration reaction. Tetrahedron. Lett. 53, 3245–3249.

26. Lathiya, D.R., Bhatt, D.V., Maheria, K.C., 2019. Sulfated fly-ash catalyzed biodiesel production from maize acid oil feedstock: a comparative study of taguchi and box-behnken design. ChemistrySelect 4, 4392–4397.

27. Lei, H., Gu, Q., 2015. Preparation of Cu-doped colloidal SiO$_2$ abrasives and their chemical mechanical polishing behavior on sapphire substrates. J. Mater. Sci.: Mater. Electron. 26, 10194–10200.

28. Maki, Y., Sato, K., Isobe, A., Iwasa, N., Fujita, S., Shimokawabe, M., Takezawa, N., 1998. Structures of H_3PO_4/SiO_2 catalysts and catalytic performance in the hydration of ethene. Appl. Catal. A 170, 269–275.

29. Mandal, P.K., Misra, A.K., 2006. $HClO_4$-SiO_2 catalyzed multicomponent reactions for the synthesis of privileged heterocyclic structures. Lett. Org. Chem. 3, 848–853.

30. Manríquez, M.E., López, T., Gomez, R., Picquart, M., Hernández-Cortez, J.G., 2004. Sol-gel silica modified with phosphate and sulfate ions. J. Non-Cryst. Solids 345–346, 643–646.

31. Mazumder, N.A., Rano, R., Sarmah, G., 2015. A green and efficient solid acid catalyst from coal fly ash for Fischer esterification reaction. J. Ind. Eng. Chem. 32, 211– 217.

32. Niknam, K., Saberi, D., Baghernejad, M., 2010. Preparation of silica-bonded S- sulfonic acid: a recyclable catalyst for the synthesis of bis-indolylmethanes. Phosphorus, Sulf. Silicon Rel. Elem. 185, 875–882.

33. Salehi, P., Ali Zolfigol, M., Shirini, F., Baghbanzadeh, M., 2006. Silica sulfuric acid and silica chloride as efficient reagents for organic reactions. Curr. Org. Chem. 10, 2171–2189.

34. Shaabani, A., Rezayan, A.H., 2007. Silica sulfuric acid promoted selective oxidation of sulfides to sulfoxides or sulfones in the presence of aqueous H_2O_2. Catal. Commun. 8, 1112–1116.

35. Tokuda, N., Takeuchi, D., Ri, S.-G., Umezawa, H., Yamabe, K., Okushi, H., Yamasaki, S., 2009. Flattening of oxidized diamond (111) surfaces with H_2SO_4/ H_2O_2 solutions. Diam. Relat. Mater. 18, 213–215.

36. Vekariya, R.H., Prajapati, N.P., Patel, H.D., 2016. Silica-supported polyphosphoric acid (PPA-SiO_2): an efficient and reusable heterogeneous catalyst for ecofriendly organic synthesis. Synthetic Commun. 46, 197–219.

37. Wang, J., Li, D., Ju, F., Han, L., Chang, L., Bao, W., 2015. Supercritical hydrothermal synthesis of zeolites from coal fly ash for mercury removal from coal derived gas. Fuel Process. Technol. 136, 96–105.

38. Wang, Q., Wei, Y., Xu, S., Zhang, M., Meng, S., Fan, D., Qi, Y., Li, J., Yu, Z., Yuan, C., He, Y., Xu, S., Chen, J., Wang, J., Su, B., Liu, Z., 2014. Synthesis of mesoporous ZSM-5 using a new gemini surfactant as a mesoporous directing agent: a crystallization transformation process. Chinese J. Catal. 35, 1727–1739.

39. Wang, S., Wu, H., 2006. Environmental-benign utilisation of fly ash as low-cost adsorbents. J. Hazard Mater. 36, 482–501.